Electron-Triggered Imine Coupling: Synthesis and Characterization of Three Redox States (0,–1,–2) of a Ni(N 2 S 2) Complex

Loïc Mangin, Yahya Albkuri, Jeffrey Ovens, Shaymaa Al Shehimy, Lhoussain Khrouz, Stephan Steinmann, Christophe Bucher, R. Tom Baker

Electron-triggered imine coupling: Synthesis and Characterization of Three Redox States (0, -1, -2) of a Ni(N_2S_2) complex

Loïc P. Mangin,[a] Yahya M. Albkuri,[a] Jeffrey S. Ovens,[b] Shaymaa Al Shehimy,[c] Lhoussain Khrouz,[c] Stephan Steinmann,*[c] Christophe Bucher,*[c] and R. Tom Baker*[a]

E-mail: rbaker@uottawa.ca, christophe.bucher@ens-lyon.fr, stephan.steinmann@ens-lyon.fr

[a] Dr. Loïc P. Mangin, Dr. Yahya M. Albkuri, Prof. Dr. R. Tom Baker
Department of Chemistry and Biomolecular Sciences and Centre for Catalysis Research and Innovation
University of Ottawa
30 Marie Curie, Ottawa, Ontario K1N 6N5, Canada
E-mail: rbaker@uottawa.ca

[b] Dr. Jeffrey S. Ovens
Faculty of Science
University of Ottawa
150 Louis Pasteur Pvt., Ottawa, Ontario K1N 6N5, Canada

[c] Shaymaa Al Shehimy, Lhoussain Khrouz, Dr. Stephan Steinmann, Dr. Christophe Bucher
ENSL, CNRS, Laboratoire de Chimie UMR 5182
46 allée d'Italie, 69342 Lyon, France
Email: christophe.bucher@ens-lyon.fr, stephan.steinmann@ens-lyon.fr

Supporting information for this article is given via a link at the end of the document.

Abstract: Metal imine-thiolate complexes, $M(NS)_2$ are known to undergo imine C-C bond formation to give $M(N_2S_2)$ complexes (M = Co, Ni) containing a redox-active ligand. Although these transformations are not typically quantitative, we demonstrate here that one-electron reduction of a related Ni bis(imine-thiolate) complex affords the corresponding paramagnetic $[Ni(N_2S_2)]^-$ anion (**2**$^{\bullet-}$) exclusively; subsequent oxidation with $[Cp_2Fe]BF_4$ then affords a high yield of neutral **2** (Cp = η^5-cyclopentadienyl). Moreover, electrochemical studies indicate that a second 1-electron reduction affords the diamagnetic dianion. Both anionic products were isolated and characterized by SC-XRD and their electronic structures were investigated by UV-vis spectroelectrochemistry, EPR and NMR spectroscopy, and DFT studies. These studies show that reduction proceeds primarily on the ligand, with $(N_2S_2)^{4-}$ containing both thiolate and ring-delocalized anions.

Introduction

First-row transition metal complexes are increasingly playing a broader role in both homo- and heterogeneous catalysis as their unique one-electron transformations continue to be more efficiently harnessed.[1] For molecular catalysts, novel transformations have been effected with the assistance of functional ligands.[2] In a recent example, the Chirik group showed that an Fe complex containing the redox-active bis(imino)pyridine ligand catalyzes both the [2+2] cycloaddition-oligomerization of 1,3-butadiene to (1,n'-divinyl)oligocyclobutane and its deoligomerization, demonstrating the first closed-loop recycling of a hydrocarbon polymer.[3]

In 1992, Kawamoto and Kushi demonstrated the thermal conversion of a Ni bis(imine-thiolate) complex, $M(NS)_2$, to its $M(N_2S_2)$ isomer via imine C-C bond formation (**Scheme 1**).[4-6] They recognized that the resulting N_2S_2 ligand was redox non-innocent and likely a dianionic ligand with two electrons in the ligand framework. Subsequent work by Wieghardt and co-workers on Fe and Co complexes applied a combination of spectroscopic, crystallographic, and computational techniques to more accurately assess the oxidation state of both the metal and the ligand (**Scheme 2**).[7-15] For the Co case they showed that intimate sharing of the electrons by the nearly isoenergetic metal and ligand orbitals prevented a clear assignment of the Co oxidation state.[14] We recently reported the synthesis and reactivity of Ni(κ^2-SNS^{Me})$_2$ (**1**) in which the imine C-phenyl substituent bears an *ortho* thioether group.[16] In this work we employ spectroelectrochemistry, NMR and EPR spectroscopy, and computational chemistry to access and characterize three stable Ni(N_2S_2) redox states derived from **1**.

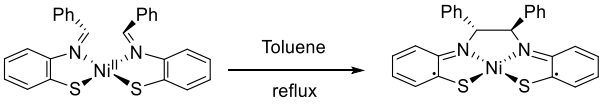

Scheme 1. Thermal conversion of $Ni(NS)_2$ to the $Ni(N_2S_2)$ complex.

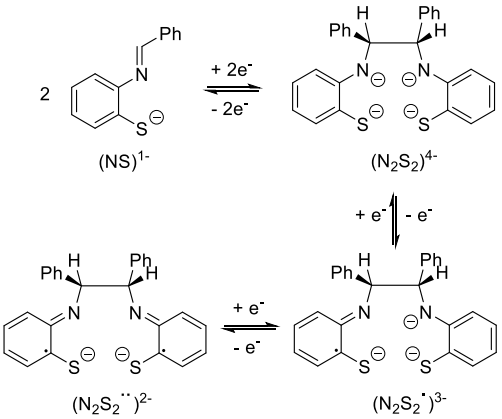

Scheme 2. Three proposed ligand redox states derived from imine C-C bond coupling of the imine-thiolate NS ligand.

Results and Discussion

Electrochemistry of Ni(κ^2-SNS^{Me})$_2$ (1)

The electrochemical properties of Ni(κ^2-SNS^{Me})$_2$ (**1**) were investigated in THF in the presence of tetra-*n*-butylammonium hexafluorophosphate (0.1 M). Initial studies revealed that the

electrochemical response depends on scan rate: the curve recorded at 10 mV·s^{-1} displays two consecutive, irreversible, reduction waves below -1 V (**Figure 1A**) while that recorded at 100 mV·s^{-1} exhibits only one broad electron reduction wave at E_{pc} = -1.125 V (**Figure 1B**). Another key feature of the CV curve shown is the fully reversible oxidation wave at ca. $E_{1/2}$ = -0.27 V, which is only observed when scanning back from -1.5 V to the initial open circuit potential. These drastic effects could be attributed to the limited stability of the oxidized and reduced species on the time scale of the CV experiment and to the existence of coupled chemical reactions yielding redox-active products. More specifically, these features are consistent with an ECE mechanism including a chemical step (C) coupled to the initial one-electron reduction (E) of **1** at E_{pc} = -1.125V, yielding a new species that can be both reduced right after **1** and oxidized at $E_{1/2}$ = -0.27 V. These data are consistent with an electron-triggered ligand dimerization of **1** to $[Ni(N_2S_2)]^-$ (**2**$^{\bullet-}$) proceeding through the unstable intermediate, $[Ni(\kappa^2\text{-}SNS^{Me})_2]^-$ (**1**$^{\bullet-}$) (**Scheme 3**).

Further support for this conclusion came from additional investigations involving quantitative electrochemical reduction of **1** monitored by electrochemical methods coupled to time-resolved *in situ* UV-vis absorption measurements (**Figure 2**). The potentiostatic coulometry experiment was carried out at a platinum plate working electrode with potential held constant at E_{app} = -1.6 V. In the first stage of the electrolysis, corresponding to addition of one electron/Ni, reduction led to the progressive disappearance of the broad MLCT band at λ_{max} = 460 nm at the expense of two bands growing in at λ_{max} = 696 and 903 nm, along with a clean isosbestic point at 581 nm, reaching maximum intensities after addition of 1e$^-$ per molecule of **1** (**Figure 2A**). Electrochemical measurements conducted in stationary and transient regimes furthermore showed that the well-defined intermediate compound **2**$^{\bullet-}$ formed in solution at this stage of the electrolysis undergoes two Nernstian electron transfers between 0 and -1.5 V: a one electron oxidation at $E_{1/2}$ = -0.27 V to **2** as well as a one-electron reduction at $E_{1/2}$ = -1.17 V to **2**$^{2-}$ (thin solid line in **Figures 3A** and **3B**). Formation of **2**$^{2-}$ directly from **1** monitored by spectroelectrochemistry showed disappearance of the bands at 696 and 903 nm with an isosbestic point at 520 nm (**Figure 2B**).

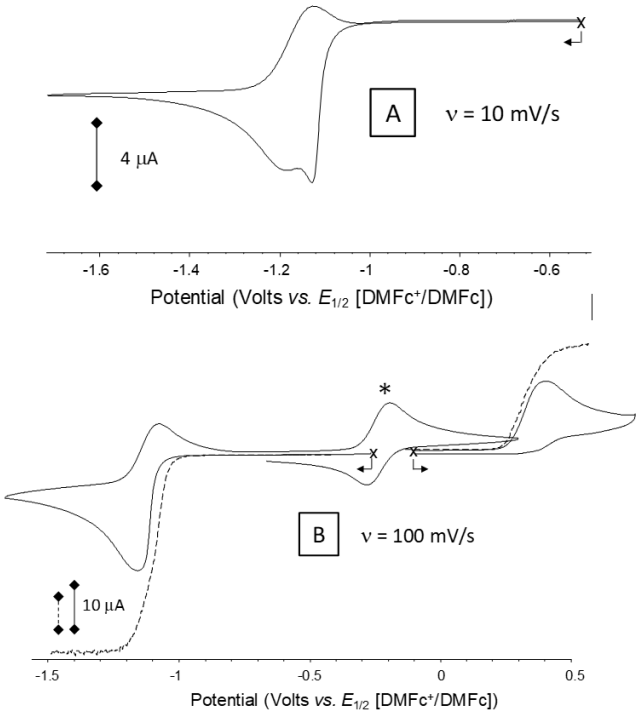

Figure 1. CV (full lines) and RDE (dashed lines) curves recorded for **1** in THF (1 mM, $TBAPF_6$ 0.1 M) at glassy carbon working electrodes at A) 10 mV·s^{-1} and B) 100 mV·s^{-1} (Ø = 3 mm, 500 rd·min^{-1} for RDE, E vs decamethylferrocene$^+$/^{0}.

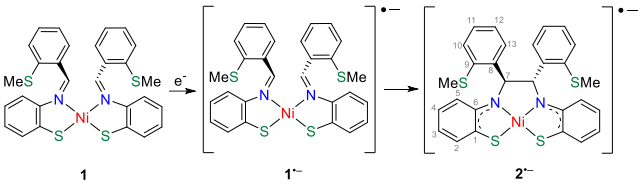

Scheme 3. Electron-triggered ligand dimerization of **1** to **2**$^{\bullet-}$ via unstable **1**$^{\bullet-}$.

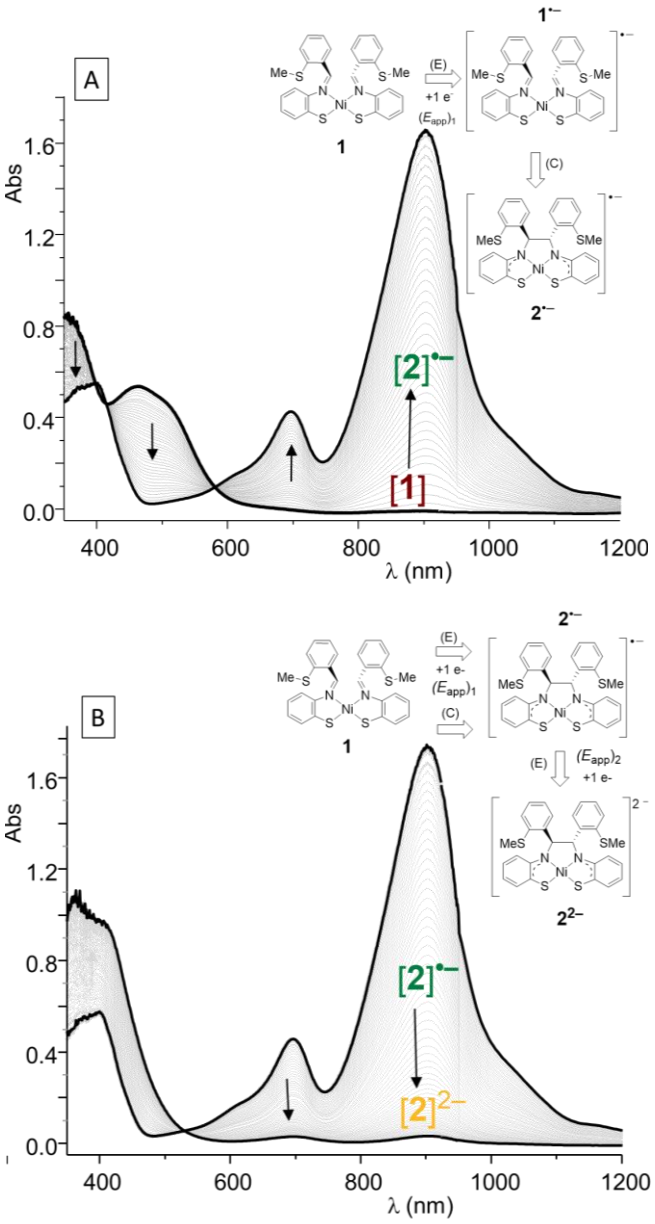

Figure 2. Superimposition of UV/Vis spectra recorded during the exhaustive reduction of **1** at E_{app} = -1.6 V after addition of A) 1 electron *per* molecule and B) 2 electrons *per* molecule. (THF + 0.1 M $TBAPF_6$, 1 mM, 10 mL, *l* = 1 mm, t ≈ 30 min, Pt).

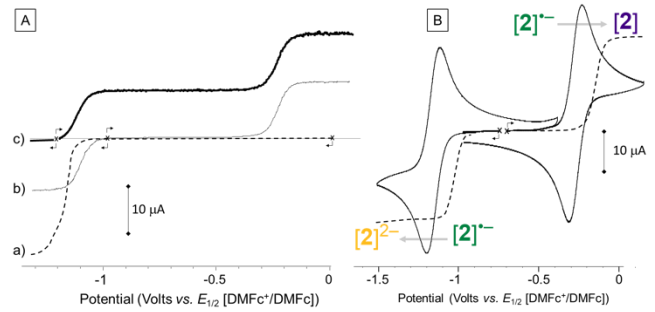

Figure 3. [A] RDE curves recorded before a) and after b) one- and c) two-electron reduction of **1** at E_{ap} = -1.4 V (Pt, 1 mM in THF+TBAPF$_6$); [B] CV and RDE curves recorded at a glassy carbon working electrode (Ø = 3 mm, 10 mV·s^{-1}, 500 rd·min^{-1}) after 1 e$^-$ reduction of **1** at E_{ap} = -1.4 V (Pt, 1 mM in THF + TBAPF$_6$). CV and RDE curves recorded at glassy carbon working electrode, Ø = 3 mm at 100 mV·s^{-1} (CV) or at 10 mV·s^{-1} / 500 rd•min^{-1} (RDE); E vs DMFc$^+$/^{0}).

Electrochemistry of Ni(N_2S_2) (2)

The electrochemistry starting with isolated **2** confirms the two reversible reductions proposed above (**Figure 4).** On the anodic side, the shape and relative position of the CV curves are consistent with two successive one-electron oxidation processes centered on both imine-thiolate moieties (**Scheme 4**). Under this assumption, the shift in potential observed between both waves can be attributed to through-bond or through-space "communication" processes occurring between both imine-thiolates, the oxidation of the first one making the oxidation of the second harder. This attribution relies on i) the number of electrons involved in these waves (2x 1e$^-$) and ii) DFT data (*vide infra*) indicating that the organic subunits of the complex are more likely to be oxidized than the metal center.

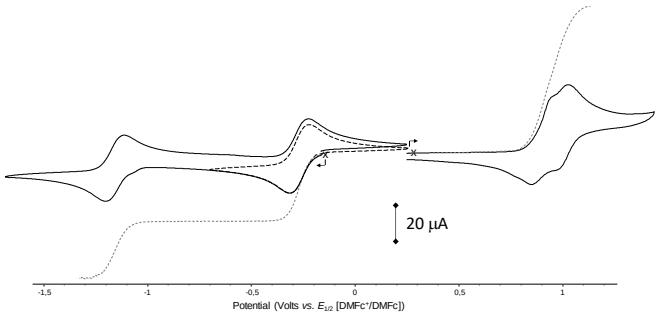

Figure 4 CV measurement of reduction and oxidation of neutral **2**. CV and RDE curves recorded in THF (1 mM, TBAPF$_6$ 0.1 M) at glassy carbon working electrode at v = 0.1 V s^{-1} (CV) or 10 mV·s^{-1} (RDE, 500 rd•min^{-1}) (Ø = 3 mm, E vs DMFc$^+$/DMFc).

The reduced species **(2)$^{\bullet-/2-}$** were further characterized by spectroelectrochemistry measurements, upon collecting time-resolved UV-vis spectra during the successive reduction of **2**. As can be seen in **Figure 5**, accumulation of **2$^{\bullet-}$** in solution during the electrolysis at E_{app} = -0.8 V led to the progressive disappearance of the broad signal centered at 834 nm at the expense of less intense ones at λ_{max} = 697 and 902 nm. Observation of a clean isosbestic point at 875 nm also confirms that no secondary reactions occur over the considered time range. Further reduction of the sample at E_{app} = -1.4 V led to the disappearance of the signals attributed to **2$^{\bullet-}$** at the expense of new bands developing at much higher energy) (λ < 500 nm) attributed to **2^{2-}**.

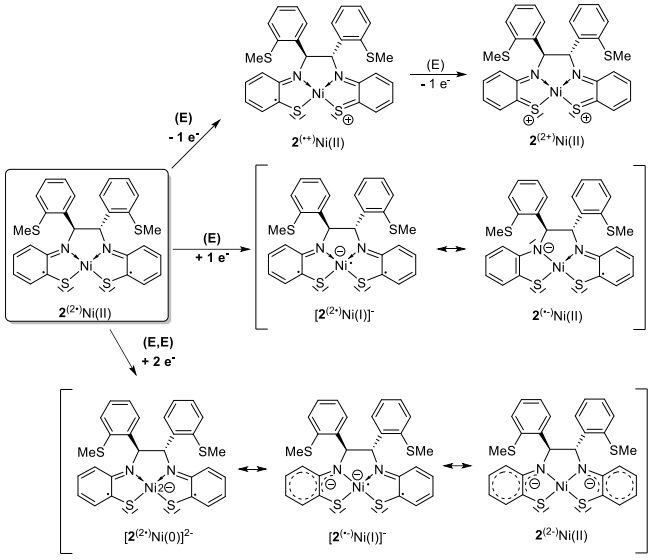

Scheme 4. Oxidation and reduction of **2**.

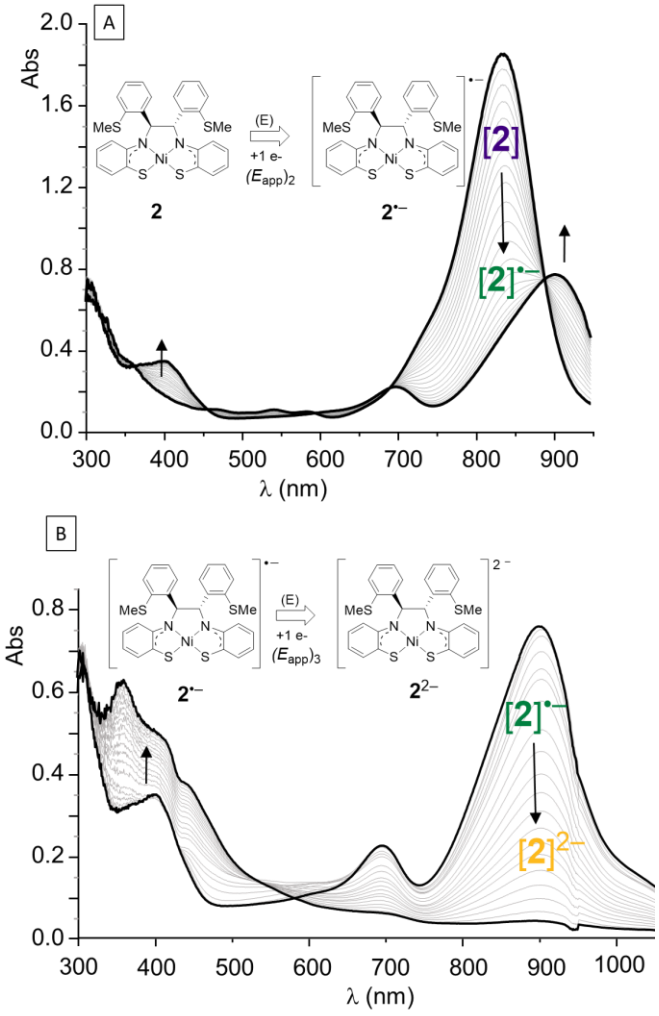

Figure 5. Superimposition of UV/Vis spectra recorded during the exhaustive reduction of **2** at A) (E_{app})$_2$ = -0.7 V (1 electron *per* mole) and B) (E_{app})$_3$ = -1.4 V (1 electron *per* molecule). (THF + 0,1 M TBAPF$_6$, 1 mM, 10 mL, l = 1 mm, t ≈ 30 min, Pt).

Step-by-step EPR Studies of Reduced 2

Formation of redox states **2**$^{\bullet-}$ and **2**$^{2-}$ was further demonstrated by EPR measurements carried out at each stage of the electrolysis. The spectrum collected after addition of one electron per Ni is shown as a full/bolded black line in **Figure 6A**. Based on simulation analyses and on experimental literature data reported for relevant Ni(I) compounds,[17-19] we assign the intense signals observed at $g_x = 1.995$ $g_y = 2.022$ and $g_z = 2.118$ to **2**$^{\bullet-}$ with an S = 1/2 spin state. This attribution was further supported by simulation studies showing that the multiplicity of the g_x signal results from hyperfine coupling with two equivalent nitrogen atoms ($a_N = 8.8$ G, full black line in (**Figure 6B**). EPR measurements carried out on the two-electron reduced complex gave a silent spectrum featuring only a residual signal attributed to traces of the Ni(I) intermediate (dashed line in **Figure 6A**). This absence of signal is in agreement with formation of diamagnetic **2**$^{2-}$.

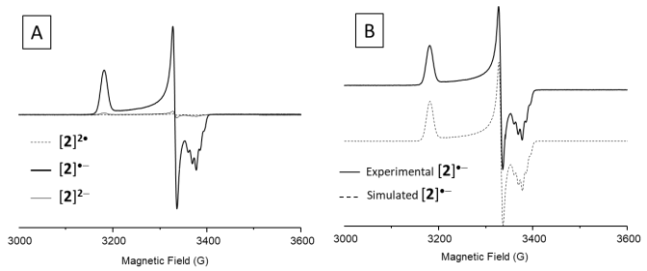

Figure 6. A) experimental X-band EPR spectra (110 K, microwave power = 6 mW; modulation amplitude = 2 G) recorded before (dashed line) and after exhaustive electrochemical reduction of **2** in THF (0.1 M $TBAPF_6$) at E_{app} = -0.8 V (bolded black line) and at E_{app} = -1.4 V (thin black line) B) experimental and simulated EPR spectra of **2**$^{2-}$.

Synthesis and Molecular Structures of Ni(N_2S_2) Complexes

Building on the above electrochemical results, we treated complex **1** in THF with one equiv of sodium-benzophenone, and the dark red mixture turned deep green within 2 h, and then deep blue overnight. Precipitation of the product led to a dark teal-blue solid, in 72% yield (**Scheme 5**), for which the ^{1}H NMR data were consistent with a paramagnetic complex, with broad signals spanning the 0-30 ppm range (**Fig. S1**). In addition, based on the signal for the SCH_3 protons, we found that the powder contains ca. 0.4 molecules of THF and 1.7 molecule Et_2O per Ni, which indicates significant alkali metal desolvation during the precipitation process. Crystallization from THF/Et_2O afforded deep blue crystals which confirmed the reduction of the complex to the $[Ni(N_2S_2)]^-$ anion, to which the counter-cation $[Na(THF)_3]^+$ is bound via the sulfur atoms of the N_2S_2 core (**Figure 9a**). We were also able to isolate the K^+ salt of the monoanion **2**$^{\bullet-}$, prepared via a similar procedure, and crystallization from THF/pentane afforded blue crystals identified as a polymeric structure of stoichiometry $[Ni(N_2S_2)K(THF)_2]_n$ in which the Ni(N_2S_2) cores are linked by $K(THF)_2$ units through S→K bonds (polymorph α, see **Fig. S39** for thermal ellipsoid plots). We also obtained from

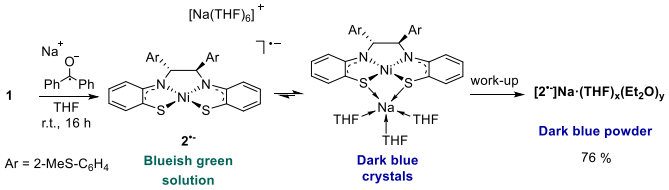

Scheme 5. Preparation of the singly reduced complex **2**$^{\bullet-}$

THF/toluene mixtures a second polymorph, β, in which the $K(THF)_2$ linkage relies on both S→K bonds and the carbon atoms of the N,S-bound six-membered ring (**Figure 9b**), suggesting that this ring has gained significant electron density upon reduction of the complex.

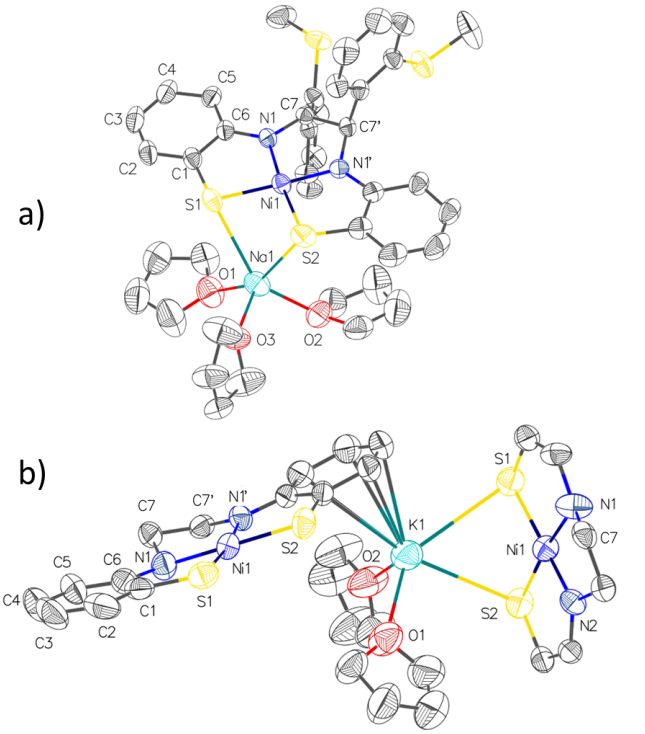

Figure 9. Molecular diagrams of (a) $[Ni(N_2S_2)][Na(THF)_3]$ and (b) polymeric β-$[Ni(N_2S_2)K(THF)_2]_n$ showing K linkage with two $[Ni(N_2S_2)]^-$ units. . Thermal ellipsoids are shown at the 50% probability level; H atoms and 2-thioanisyl fragments in (b) are omitted for clarity.

Solid state structures of Na^+- and K^+-bound **2**$^{\bullet-}$ reveal a square planar environment around the Ni center, with little to no distortion compared to neutral **2**, with τ_4 values[19] of 0.07 and 0.08, respectively, versus 0.07 for **2**, which points towards a Ni(II) center in the monoanions although the rigidity of the tetradentate ligand cannot easily accommodate the pseudo-tetrahedral geometry anticipated for d^9 centers. However, while the C7-C7' distance remains similar upon reduction, the intrinsic distortion about the two halves of the ligand (N1-C7-C7'N1' dihedral) increases significantly.

The doubly reduced analogue of **2** was obtained by treating **1** with two equiv of potassium metal in THF, resulting in a dark yellow mixture which, upon precipitation, led to a pale green solid. The latter re-dissolves in THF, MeCN or DMSO to turn back from dark yellow to orange (**Scheme 6**). The ^{1}H NMR spectrum of **(K^+)$_2$[2^{2-}]** in DMSO-d_6 shows a diamagnetic complex (**Figs. S3-S5**), as expected from loss of the EPR signal upon addition of a second

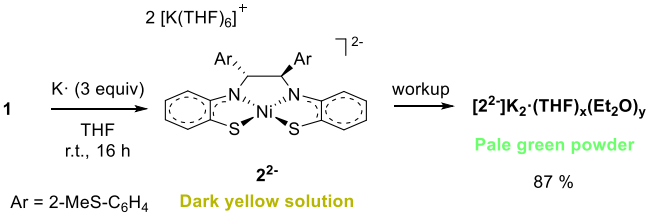

Scheme 6. Preparation of the doubly reduced complex **2**$^{2-}$

Table 1. Structural features of the alkali-bound monoanionic and dianionic Ni(N_2S_2) complexes.[a]

	Ni(N_2S_2)	**[Na(THF)$_3$][Ni(N_2S_2)]**	**β-[K(THF)$_2$][Ni(N_2S_2)]}$_n$**	**{[K_2(THF)$_{2.5}$][Ni(N_2S_2)]}$_n$**
Ni-S	2.1286(5) ; 2.1310(5)	2.1460(7) ; 2.1500(7)	2.1483(6) ; 2.1495 (6)	2.167(2) ; 2.170(2)
Ni-N	1.8119(13) ; 1.8151(14)	1.821(2) ; 1.817(2)	1.817(2) ; 1.820 (2)	1.845(6) ; 1.846(5)
S-C1	1.724(2) ; 1.722(2)	1.753(3) ; 1.739(3)	1.752(2) ; 1.755(2)	1.750(9) ; 1.746(8)
N-C6	1.354(2) ; 1.354(2)	1.356(3) ; 1.356(3)	1.369(3) ; 1.368(3)	1.346(8) ; 1.346(8)
N-C7	1.466(2) ; 1.468(2)	1.467(3) ; 1.456(3)	1.469(2) ; 1.474(2)	1.461(8) ; 1.459(8)
C1-C2	1.402(2) ; 1.410(3)	1.386(4) ; 1.396(4)	1.395(3) ; 1.394(3)	1.387(11) ; 1.388(9)
C2-C3	1.362(3) ; 1.369(4)	1.382(5) ; 1.371(6)	1.380(4) ; 1.385(3)	1.397(14) ; 1.387(12)
C3-C4	1.407(3) ; 1.386(4)	1.389(5) ; 1.379(6)	1.394(4) ; 1.397(3)	1.357(15) ; 1.363(11)
C4-C5	1.371(3) ; 1.376(3)	1.387(4) ; 1.383(4)	1.379(3) ; 1.381(3)	1.386(11) ; 1.382(9)
C5-C6	1.414(2) ; 1.417(3)	1.408(4) ; 1.414(4)	1.415(3) ; 1.411(3)	1.405(10) ; 1.419(9)
C1-C6	1.416(2) ; 1.419(3)	1.416(3) ; 1.420(4)	1.417(3) ; 1.421(3)	1.427(10) ; 1.411(9)
C7-C7’	1.558(2)	1.552(3)	1.562(3)	1.544(8)
N1-C7-C7’-N1’	14.5(2)	24.3(2)	20.2(2)	28.9(6)
τ_4	0.070	0.074	0.077	0.122

[a] None of the complexes presented herein are perfectly symmetrical, hence, two values are presented for each set of bonds: Ni-S represents Ni1-S1 and Ni1-S2 ; S-C1 represents S1-C1 and S2-C14 and N1-C7-C7’-N1’ represents N1-C7-C8-N2.

electron per complex (*vide supra*). In the powder, we also observed considerable desolvation of the K^+ ions, with ca. 0.2 molecules of THF and 1.2 molecules of Et_2O per Ni. ^{1}H NMR analysis also revealed significant shielding of the aromatic protons of the N_2S_2 core, with signals ranging from 5.35 (for C5$_{Ar}$-*H*) to 6.40 (for C2$_{Ar}$-*H*) ppm, and a notable deshielding of the signal for C13$_{Ar}$-*H*, which resonates at 9.77 ppm, most likely because it lays on top of the square plane around Ni. Unfortunately, we were not able to compare it to the neutral Ni(N_2S_2) in DMSO-d_6, because of the very low solubility of **2**. However, the same trend was observed in protio-THF in which the aromatic protons C2$_{Ar}$-*H* to C5$_{Ar}$-*H* shifted to 5.69–6.66 ppm (versus 6.69–7.69 ppm for all aromatic protons in neutral **2**) and C13$_{Ar}$-*H* was found at 9.46 ppm (**Fig. S30**). Crystallization from THF/Et_2O afforded pale green crystals, that confirmed the identity of the complex as the doubly reduced **2^{2-}** with 2:1 K:Ni stoichiometry (as [Ni(N_2S_2)][K_2(THF)$_{2.5}$], see **Figures 10a** and **10b**). In this structure, the potassium centers are partially solvated by THF molecules, bound to the sulfur donors of the N_2S_2 backbone, as well as aromatic carbon→K interactions. Namely, each arene of the N_2S_2 core is bound to one K^+, indicating strong electron density in the ligand upon two-electron reduction of complex **2**. Here again, the Ni center appears to be square planar with only a slightly higher tetrahedral distortion versus the neutral or anionic complexes (τ_4 = 0.12).

Although the geometry index varies only slightly from the neutral complex to the mono- and then to the di-anionic complexes, there are noteworthy structural features that differentiate each of the Ni(N_2S_2) redox states (**Table 1**). Upon addition of one and then two electrons, both Ni-S distances increase significantly from 2.13 Å to 2.15 and 2.17 Å, respectively. The same trend is also observed for the Ni-N distances, albeit to a lesser extent, and is more significant between the neutral and the doubly reduced complex, *i.e.*, from 1.82 Å to 1.85 Å. A close inspection of the ring C-C bond distances in complex **2** shows a bond alternation that disrupts the ring aromaticity. This feature is faithfully reproduced by the DFT calculations (see **Scheme S1**), indicating that each (NS$^{\bullet}$)$^-$ half of the N_2S_2 core around Ni is best represented by a *o*-iminothionebenzosemiquinonate π-radical ligand. In addition, the bond alternation disappears in the anionic counterparts, and direct towards a partial reduction of the ligand. This echoes the

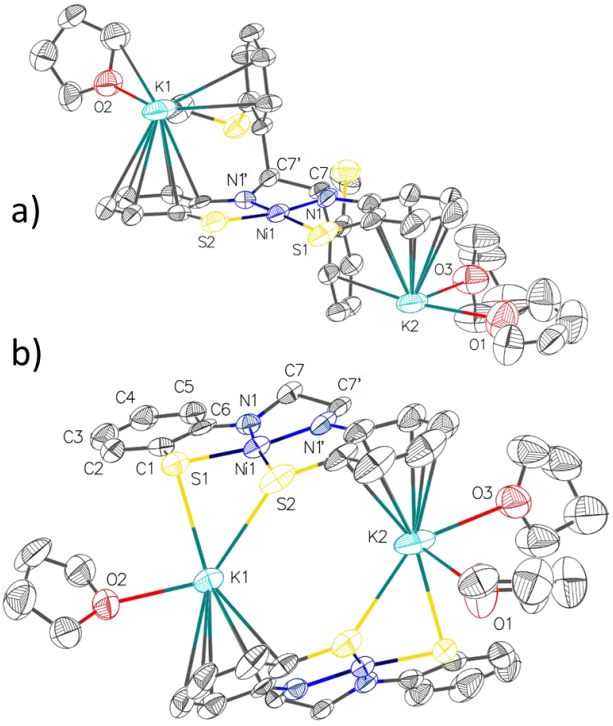

Figure 10. Molecular diagrams of polymeric [Ni(N_2S_2)K_2(THF)$_{2.5}$]$_n$ focused on (a) the [(N_2S_2)Ni]$^{2-}$ dianionic fragment; and (d) the K^+ environments. Thermal ellipsoids are shown at the 50% probability level; H atoms and 2-thioanisyl fragments are omitted for clarity.

findings by Wieghardt *et al.*, with similar neutral Co^{II}(N_2S_2) and Fe^{III}I (N_2S_2) complexes, in which the ($N_2S_2^{\bullet\bullet}$)$^{2-}$ core was found to be a dianionic open-shell singlet.[13,14] Interestingly, while the Co(N_2S_2) complex also leads to disappearance of the C-C ring bond alternation upon 1e$^-$ reduction, the Fe complex Fe^{II}(N_2S_2)(PPh_3) conserves the biradical character of its ligand. This indicates that reduction of the iron complex is metal-centered, while that of the cobalt complex is primarily ligand-centered, giving species of the type Fe^{II}[($N_2S_2^{\bullet\bullet}$)$^{2-}$] and Co^{III}[($N_2S_2^{\bullet}$)$^{3-}$]. In the case of our singly reduced Ni complex, the DFT studies (*vide infra*) support a weak Ni(I) character, while the lack of bond alternation and the arene→K^+ interactions support a reduction of

Table 2. Structural features of the free singly and doubly reduced Ni(N_2S_2) complexes.[a]

	Ni(N_2S_2)	**[Na(THF)$_6$][Ni(N_2S_2)]**	**[K(18C6)(THF)][Ni(N_2S_2)]**	**[K(18C6)(sol)$_x$]$_2$[Ni(N_2S_2)]**
Ni-S	2.1286(5) ; 2.1310(5)	2.154(2) ; 2.144(2)	2.1561(4) ; 2.1477(3)	2.1872(5) ; 2.1839(5)
Ni-N	1.8119(13) ; 1.8151(14)	1.821(7) ; 1.822(6)	1.8274(9) ; 1.8327(9)	1.8518(13) ; 1.8407(14)
S-C1	1.724(2) ; 1.722(2)	1.765(9) ; 1.736(10)	1.7493(13) ; 1.7437(13)	1.7582(2) ; 1.757(2)
N-C6	1.354(2) ; 1.354(2)	1.376(10) ; 1.363(10)	1.3643(14) ; 1.3622(13)	1.355(2) ; 1.366(2)
N-C7	1.466(2) ; 1.468(2)	1.494(9) ; 1.474(10)	1.4629(13) ; 1.4687(13)	1.457(2) ; 1.451(2)
C1-C2	1..402(2) ; 1.410(3)	1.417(12) ; 1.376(12)	1.398(2) ; 1.398(2)	1.387(2) ; 1.385(2)
C2-C3	1.362(3) ; 1.369(4)	1.398(14) ; 1.402(13)	1.379(2) ; 1.386(2)	1.394(3) ; 1.376(5)
C3-C4	1.407(3) ; 1.386(4)	1.378(14) ; 1.338(13)	1.389(2) ; 1.396(2)	1.386(3) ; 1.365(5)
C4-C5	1.371(3) ; 1.376(3)	1.368(12) ; 1.368(11)	1.386(2) ; 1.385(2)	1.393(3) ; 1.402(3)
C5-C6	1.414(2) ; 1.417(3)	1.369(11) ; 1.422(11)	1.407(2) ; 1.410(2)	1.404(3) ; 1.404(2)
C1-C6	1.416(2) ; 1.419(3)	1.403(11) ; 1.422(11)	1.418(2) ; 1.424(2)	1.429(2) ; 1.419(3)
C7-C7′	1.558(2)	1.533(10)	1.5525(14)	1.558(2)
N1-C7-C7′-N1′	14.5(2)	35.0(8)	32.5(1)	25.4(2)
τ_4	0.070	0.088	0.079	0.098

[a] None of the complexes presented herein are perfectly symmetrical, hence, two values are presented for each set of bonds: Ni-S represents Ni1-S1 and Ni1-S2 ; S-C1 represents S1-C1 and S2-C14 and N1-C7-C7'-N1' represents N1-C7-C8-N2.

the ligand. In fact, complex $\mathbf{2}^{\bullet-}$ cannot be described by discrete oxidation states of either the ligand or the metal, and is somewhere between the two limiting resonance formulae $Ni^{I}[(N_2S_2^{\bullet\bullet})^{2-}]$ and $Ni^{II}[(N_2S_2^{\bullet})^{3-}]$. On the other hand, further reduction towards $\mathbf{2}^{2-}$ is mostly ligand centered, with a tetraanionic, closed shell, $(N_2S_2)^{4-}$ core as depicted in **Scheme 2**, where the charge on the N and S atoms is delocalized on the aromatic rings, as supported by XRD, NMR and DFT studies (see **Figure 1A** below).

In order to better represent the structural features observed during the electrochemical experiments, in which the mono- and di-anion are generated *in situ* without the possibility of binding counter cations through S or arene donors, we sought to replace the alkali cations to generate free ions $\mathbf{2}^{\bullet-}$ and $\mathbf{2}^{2-}$. First, we attempted ion exchange experiments for $\mathbf{2}^{2-}$, but exchanging the K^+ for $^n Bu_4N^+$ did not allow us to obtain crystals, in spite of the colour change observed (from yellow to orange) and the precipitation of a fine salt (presumed to be KBr). We proceeded next to treating the K salt of $\mathbf{2}^{2-}$ with [PPh_4]Cl. Although a colour change to dark brown was observed, the reaction mixture did not appear clean by ^{31}P NMR, indicating that the reaction was not limited to ion exchange. Filtration and cooling of the reaction mixture afforded dark brown crystals of **3**, identified as the PPh_4^+ salt of a mono-anion featuring the Ni(N_2S_2) core with one of the imine nitrogens now protonated (**Scheme 7**, **Figure 11**). We could not determine, however, the proton source nor characterize the side products formed in this reaction.

We thus moved to a different strategy, consisting of trapping the potassium ions with the crown ether 18-crown-6 (18C6), which was successful. Adding 1.1 equiv of the crown ether to {[Ni(N_2S_2)][K(THF)$_2$]}$_n$ turned the solution from deep blue to deep green. This recalled the colour of the crystals obtained for the fully dissociated Na^+ salt of the monoanion, Ni(N_2S_2)][Na(THF)$_6$], which were unfortunately not of sufficient quality to obtain a

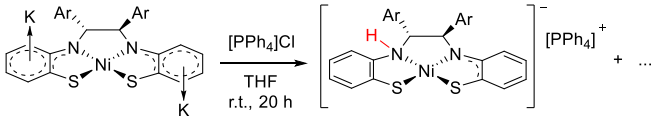

Scheme 7. Attempted cation exchange gives N-protonation of the N_2S_2 ligand.

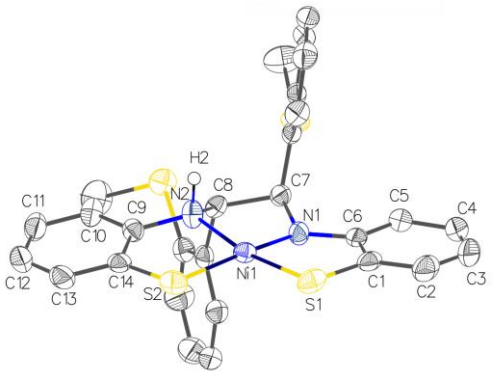

Figure 11 Molecular diagram of the {Ni[N(NH)S_2]}$^-$ anion of the $[PPh_4]^+$ salt (**3**). Thermal ellipsoids are shown at the 50% probability level. Hydrogen atoms were refined via the riding model and the counter-cation $[PPh_4]^+$ and co-crystallized MeCN are omitted for clarity.

complete data set and determine accurate parameters. On the other hand, capturing K^+ ions with 18C6 afforded good quality, deep green plates in which the $[K(18C6)(THF)]^+$ cation does not interact with either the sulfurs or ring carbons of the N_2S_2 ligand. This strategy was also efficient for the isolation of a free form of $\mathbf{2}^{2-}$, in which the dark yellow solution rapidly turned orange-red, and the product crystallized rapidly upon letting the reaction stand at room temperature. The very small needles were extremely air sensitive and decomposed quickly under the X-ray beam at 200 K, but we were able to determine the connectivity, in which there were no S→K or arene→K bonding, and two $[K(18C6)(THF)]^+$ units were separated by a disordered THF molecule binding either one or the other potassium, causing a poor thermal stability of the crystals. We solved this issue by repeating the cation trapping experiment, in THF containing 20% v/v dioxane, and the latter successfully replaced the disordered THF, affording more robust crystals.

Structural analysis of the free mono- and di-anion (**Table 2**) revealed similar features to their alkali-bound counterparts, namely a square planar environment that does not deviate much from that of complex **2**, pointing to a d^8 Ni^{II} center in all three redox states of the complex. The lengthening of the Ni-S and Ni-N bond distances upon 1- and 2-electron reductions is more evident in this series of structures, in accordance with stronger electronic

repulsion between the reduced ligand and the Ni(II) center. In addition, we clearly observe in the iminothiolate an increase in the S-C bond length, from 1.72 to 1.75 to 1.76 Å indicating an increased arylthiolate character of the S donors upon reduction, while the N-C bonds do not increase significantly.

High Yield Synthesis of 2

As mentioned previously, heating **1** in refluxing toluene gave **2** in low yield as formation of by-products necessitated a chromatographic separation to obtain a pure product. Similar results were obtained by Kawamoto and Kushi using the $Ni(NS)_2$ complex shown in **Figure 1** (56% yield).[5] As one-electron reduction of **1** affords $\mathbf{2}^{\bullet-}$ as the only product, subsequent chemical oxidation should afford neutral **2** in high yield. Indeed, treatment of $\mathbf{2}^{\bullet-}$ with $[Fe(\eta^5\text{-}C_5H_5)_2][BF_4]$ in THF gave **2** exclusively (see **Fig S32**) in good yields after a simple work-up. We thus sought to run the sequential reduction-imine coupling-oxidation process in a one-pot manner, to obtain **2** directly from **1**. As a result, treating **1** with 1.1 equiv of potassium metal to generate the radical anion, and re-oxidation with 1.3 equiv $[Fc^+][BF_4^-]$ allowed us to obtain neutral **2** in 89% yield (**Scheme 8**).

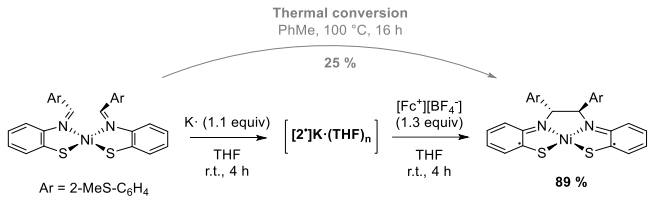

Scheme 8. One-pot reduction-imine coupling-oxidation strategy for the conversion of **1** → **2**

DFT Calculations of $Ni(SNS)_2$ (1) and $Ni(N_2S_2)$ Redox States [$\mathbf{2}^{0/1-/2-}$]

Density functional theory computations have been performed to shed more light on the electronic structures, reactivity and spectroscopic properties of **1** and $\mathbf{2}^{0/\bullet-/2-}$. By analogy to the complexes described by Wieghardt *et al.*,[12] the ground state of **2** is an open-shell singlet, while **1** is a closed shell complex. The optimized geometries are very similar to the crystal structures (**Figure S42**). The geometry of transient $\mathbf{1}^{\bullet-}$ shows more conformational flexibility with a near tetrahedral conformer being only 1.7 kcal/mol higher in energy than the near square-planar one. The oxidation of **1** leads to a doublet ground state at a potential of 0.9 V *vs.* SHE. The oxidation is centered on the organic ligand, as clearly visible in the density-difference with respect to the neutral complex shown in **Figure 12A**. A second oxidation process is predicted to occur at ca. +1.6 V vs SHE, involving oxidation of the uncoordinated thioether sulfur. This latter finding is not in agreement with the experimental data displayed in **Figure 4**, showing two successive and very close one-electron oxidations in the accessible potential range.

The first reduction of **2** occurs at -0.4 V vs. SHE, generating a doublet ground-state. The charge is mostly accumulating on the nitrogen atoms (**Figure 12B**), with the spin-density being dominant on Ni, in agreement with the ESR measurements. This observation is to be put into perspective with the open-shell singlet ground state of the neutral complex: In $\mathbf{2}^{\bullet-}$, Ni(II) is not reduced in terms of its charge, but acquires a Ni(I) character in terms of its spin-density, which is no longer delocalized on the ligand, although the coordinated N and S atoms each contribute to about one third of the spin polarization observed on the Ni center. A second reduction (at -1.7 V vs. SHE) generates a closed-shell dianion, where the additional charge is located on Ni, N and, to a minor extent, on the mercapto-aniline ligand. The reduction of **1** also leads to a doublet, but the additional charge is mostly located on the C=N double bond of one of the imine moieties (See **Fig. S43**), with the largest contribution on the carbon atom. In other words, the Ni center is barely involved in the observed redox-chemistry in terms of charge, suggesting it maintains a dominant Ni(II) character. However, the spin-population is non-negligible in the $\mathbf{2}^{\bullet-}$ species, reminiscent of a weak Ni(I) character.

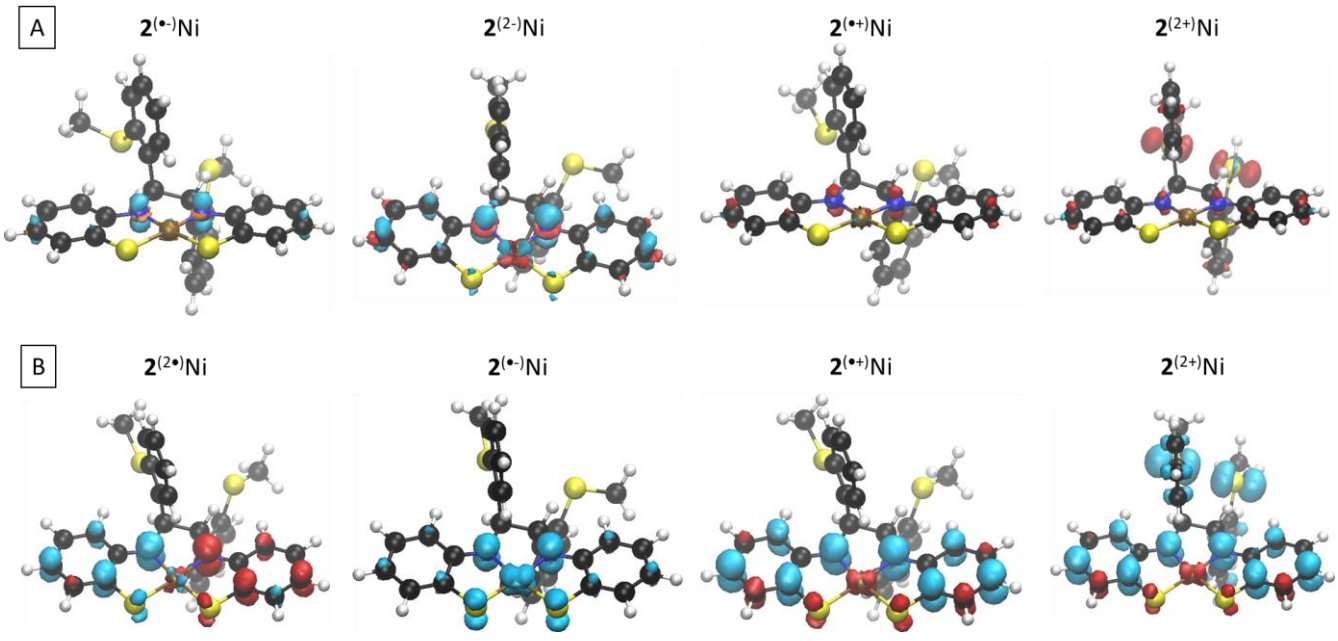

Figure 12. A: Isodensity surfaces (0.005 a.u.) of the charge difference of various complexes with respect to the neutral complex. Charge accumulation and depletion are depicted in blue and orange, respectively. B: Spin-density iso-surfaces (0.005 a.u.) of the monoanionic, neutral and cationic $Ni(N_2S_2)$ compounds; blue α-electron excess, red: β-electron excess.

DFT Calculations of Intramolecular C-C Bond Formation From 1 and $1^{\bullet-}$

We also studied the electron-triggered coupling reaction with DFT. The transition state for the C-C bond formation has been identified for both the neutral and radical anion states (**Figure 13**). The geometry of this TS is very similar in both cases, except that the forming C-C bond is 2.24 Å in the radical anion, while it is shortened to 2.05 Å in the neutral complex. The activation energy of 17.1 kcal/mol in the radical anion is compatible with the reactivity discussed in the experimental part, especially since $\mathbf{2}^{\bullet-}$ is 21.2 kcal/mol more stable than $\mathbf{1}^{\bullet-}$, revealing a significant thermodynamic driving force. This contrasts with the situation for neutral **1** in which not only is the barrier (31.4 kcal/mol) excessively high at room temperature, but also the reaction energy shows a complete reversal: **1** is found 5.6 kcal/mol more stable than **2**.

TD-DFT Studies of Three Redox States of 2.

Time-dependent density functional theory (TD-DFT) was applied to investigate the spectroscopic properties of **2**, $\mathbf{2}^{\bullet-}$ and $\mathbf{2}^{2-}$. The computed spectra are summarized in (**Figure 13**). A qualitative agreement with experiment is obtained: The most intense transition in the visible region is located at 615 and 763 nm for the neutral and radical anion, respectively, while the dianion has no transitions in this region. The nature of these transitions has been characterized via the corresponding natural transition orbitals, shown in (**Figure 14**). They reveal a mixed metal/ligand character, i.e., the electron is delocalized both in the ground and excited state across the square planar complex. The strong involvement of the metal center in this transition rationalizes the absence of the corresponding transition for $\mathbf{2}^{2-}$ in which the electrons are more delocalized between the metal and the N_2S_2 ligand rings.

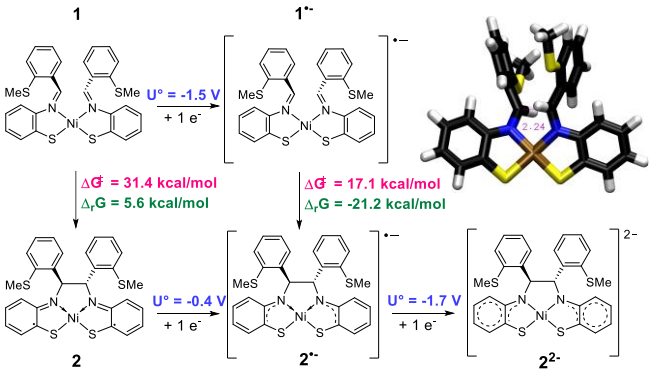

Figure 13. Summary of theoretical results at the PBE0/def2-TZVP, SMD(THF) level of theory. U°: vs SHE; the value for ferrocene/ferrocenium is, at the same level of theory, equal to 0.8 V. Top right: Transition state for the C-C bond formation in the radical anion state. In the neutral state, the geometry is very similar, except that the forming C-C bond is reduced to 2.05 Å.

Conclusions

Employing a combination of CV, rotating disk electrode and controlled potentiometry, we showed that reduction of Ni bis(thiolate) complex **1** led to reductive coupling of the imines, forming exclusively paramagnetic complex $\mathbf{2}^{\bullet-}$ that contains the redox-active $(N_2S_2)^{2-}$ ligand. Moreover, it can be reduced by a second e^- to form diamagnetic $\mathbf{2}^{2-}$. Furthermore, $\mathbf{2}^{\bullet-}$ undergoes reversible oxidation and reduction, providing three different redox states that have been isolated and characterized. Although the valence electrons are delocalized between the metal and ligand orbitals in both ground and excited states, the first reduction of the complex leads to a species of mixed Ni(I)/Ni(II) character. For the second reduction, spectroscopic data point towards a reduction of the ligand as a tetraanionic $(N_2S_2)^{4-}$ core chelating a Ni(II) center. Finally, the electrochemical measurements allowed us to develop an efficient one-pot reduction-oxidation process for the dimerization of imine-thiolate ligands around the nickel. We hope that these findings will allow more efficient preparation of metal complexes bearing redox active ligands, via chemical steps coupled to electron transfers.

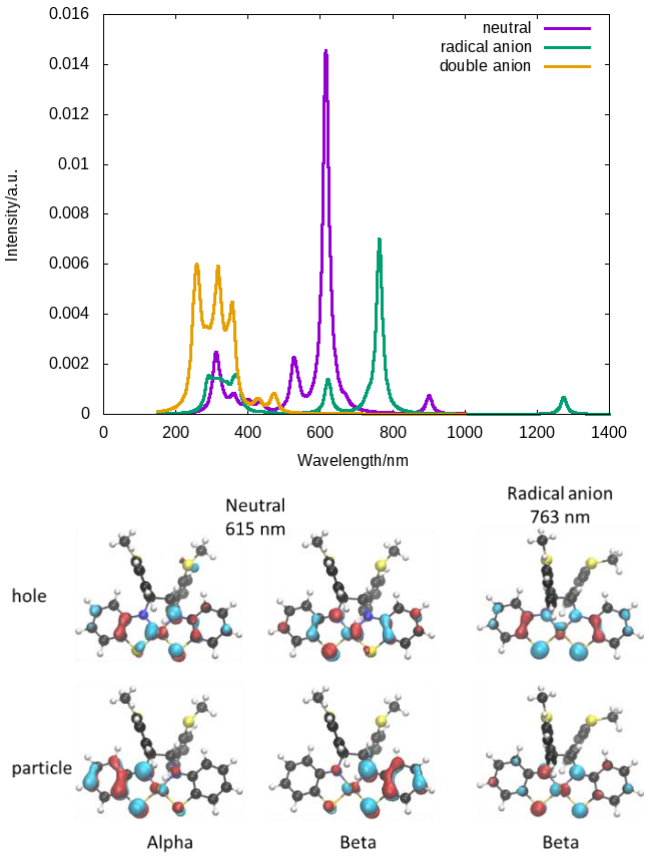

Figure 14. Left: UV-Vis spectrum for **2**, $\mathbf{2}^{\bullet-}$ *and* $\mathbf{2}^{2-}$ at the TD-PBE0/def2-TZVP level of theory. Right: Isosurfaces (0.05 a.u.) for the dominant natural transition orbitals for the hole (top row) and particle (bottom row) for the most intense transition. For $\mathbf{2}^{\bullet-}$ only the beta electrons participate significantly in the corresponding transition.

Experimental Section

General Considerations

Synthetic chemistry was carried out under nitrogen, using an MBraun glovebox and standard Schlenk techniques. Solvents were dried on columns of activated alumina using a MBraun solvent purification system, and stored over 4 Å molecular sieves. THF was further distilled on sodium-benzophenone and stored over 4 Å molecular sieves. NMR solvents were degassed by 3 freeze-pump-thaw cycles and dried over molecular sieves. Sodium, potassium, benzophenone naphthalene, ferrocenium tetrafluoroborate (technical grade) were obtained from Aldrich and used as received. 18-crown-6 was obtained from Aldrich and

recrystallized from hot acetonitrile and dried under vacuum. Complex **1** was prepared as previously reported.[15] NMR spectra were recorded at room temperature on a 600 MHz Bruker Avance III spectrometer equipped with a cryoprobe cooled to liquid N_2, and referenced to the solvent residual protons (C_6D_6, 7.16; $(CD_3)_2SO$, 2.50; $CDCl_3$, 7.26 ppm) and the solvent ^{13}C signal (C_6D_6, 128.06; $(CD_3)_2SO$, 39.52; $CDCl_3$, 77.16 ppm) with respect to tetramethylsilane at δ 0 ppm. The numbering for carbon assignments follows the order depicted in **Scheme 3**.

Electrochemistry

Electrochemical studies were performed in a glovebox (Jacomex) (O_2 < 1 ppm, H_2O < 1 ppm) with a home-designed 3- electrode cell. Cyclic voltammetry (CV) curves were recorded using a SP300 Biologic potentiostat. All studies were conducted in a standard one-compartment, three-electrode electrochemical cell using an automatic ohmic drop compensation procedure. Vitreous carbon (Ø = 3 mm) working electrodes (ALS instruments) were systematically polished with 2 mm diamond paste (PRESI SA) before recording. The non-aqueous reference electrode (ALS Instruments) was made of a silver wire dipped in a $AgNO_3$ solution (10^{-2} M + TBAP 10^{-1}M in CH_3CN). The counter electrode was a platinum wire and ferrocene or decamethylferrocene served as internal reference. THF (anhydrous, ≥99.9%, inhibitor-free) was purchased from Aldrich and further dried on activated alumina before use. Tetrabutylammonium hexafluorophosphate ($TBAPF_6$) was synthesized from tetra-*n*-butylammonium hydroxide and HPF_6, recrystallized several times from EtOH/H_2O and then dried under vacuum at 60°C for 24 h before use. Spectroelectrochemical (SEC) measurements were carried out in a "thin layer" (0.5 mm) SEC quartz cell (ALS Co) connected to a Biologic ESP-300 potentiostat equipped with a 1 A/48 V booster and a linear scan generator. Absorption measurements were carried out in remote mode with the SEC cell coupled to an MCS 500 UV-NIR Zeiss spectrophotometer through optical fibers. All measurements were carried out at room temperature in THF (anhydrous, 99.9% Acroseal) using $TBAPF_6$ as the electrolyte (0.2 M). The Ag^+/Ag reference electrode was made of a silver wire immersed in a solution containing a known concentration of Ag^+ ($AgNO_3$ (10^{-2} M) + tetrabutylammonium perchlorate (0.1 M) in THF). The counter electrode was a large surface platinum grid isolated from the main solution through a home-made electrolytic bridge.

Computational Details

All computations were performed with Orca 4.2.1.[21] (See Table S5 for examples of input lines). For singlet species, we have tested the existence of broken-symmetry solutions, but only compound **2** turned out to have such a character. The adopted density functional was PBE0-D3[22] applied in conjunction with the def2-TZVP basis set.[23] The RIJCOSX option was activated to accelerate the computations. The numerical grid quality was increased with respect to the default and set to Grid6 and GridX6. The SMD implicit solvent model was used with parameters corresponding to THF.[24] TD-DFT computations applied the Tamm-Dancoff approximation[25] and solved for 50 states.

Crystallization Details

The new polymorph (β) of the previously reported **1** (polymorph α) was obtained from vapour diffusion of hexanes into a benzene solution; **[2]Na(THF)$_3$** was crystallized from a concentrated THF solution at –35 °C, **[2][Na(THF)$_6$]** from layering a THF solution with hexanes at r.t.; **{[2]K(THF)$_2$}$_n$** from a THF/toluene solution at –35 °C for the polymorph β supported by arene→K interactions, and by vapour diffusion of pentane into a THF solution at r.t. for the polymorph α; and **{[2]K$_2$(THF)$_{2.5}$}$_n$** from vapour diffusion of Et_2O into a THF solution at –35 °C. **[(N_2S_2(H))Ni][PPh_4]** was obtained from the crude reaction mixture in MeCN cooled to –35 °C. Crystals of **[2][(18C6)K(THF)]** were obtained by adding 1.1 equiv 18-crown-6 to a solution of **[2]K(THF)$_x$** in THF and leaving the mixture evaporate slowly under inert atmosphere. Crystals of **[2][(18C6)K(THF)$_2$][(18C6)K(THF)(dioxane)$_{0.5}$]** were obtained from layering a solution of **[2]K$_2$(THF)$_x$** in 1:4 dioxane:THF with a solution of 2.2 equiv 18-crown-6 in THF at room temperature.[26]

X-ray Crystallographic Details

Crystallographic data collection and processing were performed at the X-ray Core Facility at the University of Ottawa. Crystals were mounted on MiTeGen sample holders using Parabar oil. Data were collected on a Bruker Smart Apex or Bruker Kappa Apex diffractometer equipped with an ApexII CCD detector and a sealed-tube Mo K source (λ = 0.71073 Å). During collection, the crystal was cooled to 200 K. Raw data collection and integration were performed with the Apex3 software package from Bruker.[27] Initial unit cell parameters were determined from 36 data frames from selected ω scans. Semi-empirical absorption corrections based on equivalent reflections were applied using SADABS or TWINABS.[28] Systematic absences in the diffraction dataset and unit cell parameters were consistent with the space group determined via the XPREP program.[29] Hydrogen atoms on carbons were placed geometrically and refined using the riding model, all other hydrogen atoms were placed via the difference map and refined freely. Data collection and structure refinement details are provided in **Tables S1-S3**.

Synthesis of Ni(N_2S_2)Ni in Three Redox States

*Synthesis of **[2]**Na·(THF)$_x$(Et$_2$O)$_y$:* To a mixture of 575 mg **1** (1.0 mmol) in 12 mL of THF was added dropwise 1 equiv of sodium-benzophenone ketyl prepared *in-situ* from 23 mg of sodium metal (1.0 equiv) and 200 mg of benzophenone (1.1 equiv) in 5 mL of THF. The mixture rapidly turned from brown-red to green and then overnight to deep blue-green. The THF was then removed under vacuum and the dark-blue sticky residue was treated with 8 mL of toluene and then 20 mL of Et_2O, and the precipitate was triturated for 30 min at r.t. Filtration through a glass frit, washing with 2 x 5 mL of Et_2O and drying under vacuum at r.t. afforded 574 mg of a dark blue solid. Quantitative ^1H NMR indicated the presence of 1.7 molecules of Et_2O and 0.4 molecules of THF per nickel (yield: 76%).[20] ^1H NMR (600 MHz, C_6D_6): δ 2.2 (br s), 3.2 (br s, SCH_3), 5.3 (br s), 6.8 (br s), 8.3 (br s), 10.0 (br s), 12.0 (br s), 15.3 (br s), 20.6 (br s), 30.1 (br s).

Synthesis of [2]K$_2$·(THF)$_x$(Et$_2$O)$_y$: To 230 mg of **1** (0.40 mmol) in 10 mL of THF was added 47 mg potassium metal (1.20 mmol, 3.0 equiv) in 1-2 mm pieces, and the mixture was stirred overnight at room temperature, during which time it turned from brown-red to dark blue-green to dark yellow. After filtration, the THF was removed under vacuum and the pale green residue was re-

treated with 5 mL of THF, and 25 mL of Et_2O was added to complete precipitation, followed by trituration at r.t. for 10 min. Filtration through a glass frit, washing with 2 x 5 mL of Et_2O and drying under vacuum at r.t. afforded 260 mg of a pale green solid. Quantitative ^{1}H NMR revealed the presence of 1.17 molecules of Et_2O and 0.16 molecules of THF per nickel (yield: 87%). ^{1}H NMR (600 MHz, 20 °C, DMSO-d_6): δ 2.44 (s, 6H, SCH_3), 4.24 (s, 2H, N-C7-*H*), 5.35 (d, 2H, C5$_{Ar}$-*H*, $^3J_{HH}$ = 7.8), 5.49 (t, 2H, C3$_{Ar}$-*H*, $^3J_{HH}$ = 7.0), 5.91 (t, 2H, C4$_{Ar}$-*H*, $^3J_{HH}$ = 7.1), 6.40 (d, 2H, C2$_{Ar}$-*H*, $^3J_{HH}$ = 7.0), 7.02 (t, 2H, C12$_{Ar}$-*H*, $^3J_{HH}$ = 7.5), 7.06 (td, 2H, C11$_{Ar}$-*H*, $^3J_{HH}$ = 7.5, $^4J_{HH}$ = 1.7), 7.15 (d, 2H, C10$_{Ar}$-*H*, $^3J_{HH}$ = 7.5), 9.77 (dd, C13$_{Ar}$-*H*, $^3J_{HH}$ = 7.4, $^4J_{HH}$ = 1.3). ^{13}C NMR (150.90 MHz, 20 °C, DMSO-d_6): δ 17.07 (s, 2C, S*C*H$_3$), 69.96 (s, 2C, N-*C*7-H), 104.94 (s, 2C, *C*5$_{Ar}$-H), 106.57 (s, 2C, *C*3$_{Ar}$-H), 118.91 (s, 2C, *C*4$_{Ar}$-H), 124.21 (s, 2C, *C*12$_{Ar}$-H), 125.11 (s, 2C, *C*10$_{Ar}$-H), 125.72 (s, 2C, *C*11$_{Ar}$-H), 125.77 (s, 2C, *C*2$_{Ar}$-H), 128.21 (s, 2C, *C*13$_{Ar}$-H), 135.89 (s, 2C, *C*9$_{Ar}$-SMe), 137.92 (s, 2C, *C*1$_{Ar}$-S), 147.57 (s, 2C, *C*8$_{Ar}$-C$_{sp^3}$), 159.12 (s, 2C, *C*6$_{Ar}$-N).

*Oxidation of the singly reduced complex to Ni(N_2S_2) (**2**):* To a solution of 151 mg of [**2**]Na·(THF)$_x$(Et$_2$O)$_y$ (0.20 mmol) in 10 mL of THF was added 60 mg of ferrocenium tetrafluoroborate (0.22 mmol, 1.1 equiv) in one portion. The initially blue-green mixture turned dark violet over 30 min, and was stirred overnight at room temperature. The volatiles were evaporated under vacuum, and the residue extracted with 2 x 8 mL of DCM and filtered through a glass frit. Evaporation of the DCM and washing the solid residue with 2 x 5 mL of Et_2O afforded 88 mg of a dark purple solid (yield: 76%). The ^{1}H NMR spectrum in C_6D_6 matched that of the thermally generated complex,[14] and showed the product to be > 99.5% pure. ^{1}H NMR (600 MHz, 20 °C, $CDCl_3$): δ 2.68 (s, 6H, SCH_3), 6.73 (s, 2H, N-C7-*H*), 6.83 (t, 2H, C12$_{Ar}$-*H*, $^3J_{HH}$ = 7.6), 7.02 (t, 2H, C4$_{Ar}$-*H*, $^3J_{HH}$ = 8.0), 7.12 (d, 2H, C13$_{Ar}$-*H*, $^3J_{HH}$ ≈ 8.0, overlapping with δ 7.13), 7.13 (t, 2H, C3$_{Ar}$-*H*, $^3J_{HH}$ ≈ 7.0, overlapping with δ 7.12), 7.19 (t, 2H, C11$_{Ar}$-*H*, $^3J_{HH}$ = 7.9), 7.41 (d, 2H, C10$_{Ar}$-*H*, $^3J_{HH}$ ≈ 7.5, overlapping with δ 7.42), 7.42 (d, 2H, C5$_{Ar}$- *H*, $^3J_{HH}$ ≈ 8.5, overlapping with δ 7.41), 7.69 (d, 2H, C2$_{Ar}$-*H*, $^3J_{HH}$ = 8.3). ^{13}C NMR (150.90 MHz, 20 °C, $CDCl_3$): δ 18.11 (s, 2C, S*C*H$_3$), 78.47 (s, 2C, N-*C*7-H), 120.58 (s, 2C, *C*5$_{Ar}$-H), 123.03 (s, 2C, *C*3$_{Ar}$-H), 125.89 (s, 2C, *C*13$_{Ar}$-H), 126.34 (s, 2C, *C*12$_{Ar}$-H), 127.62 (s, 2C, *C*10$_{Ar}$-H), 127.96 (s, 2C, *C*4$_{Ar}$-H), 128.63 (s, 2C, *C*11$_{Ar}$-H), 131.57 (s, 2C, *C*2$_{Ar}$-H), 137.23 (s, 2C, *C*9$_{Ar}$-SMe), 142.33 (s, 2C, *C*8$_{Ar}$-C$_{sp^3}$), 160.68 (s, 2C, *C*6$_{Ar}$-N), 161.18 (s, 2C, *C*1$_{Ar}$-S).

*High yield one-pot conversion of **1**→**2**:* In a 20 mL vial containing 144 mg of **1** (0.25 mmol) was added 6 mL of THF followed by 12 mg of potassium metal (0.28 mmol, 1.1 equiv) in 1 mm pieces. The mixture was stirred at room temperature for 4 h until all the potassium has reacted. To the resulting dark greenish-blue solution was added 89 mg of ferrocenium tetrafluoroborate (0.33 mmol, 1.3 equiv) in one portion, along with 4 mL of THF. After 4 h, the dark violet mixture was evaporated, and the residues extracted with 15 mL of DCM, filtered through a glass frit and the solid washed with 2 x 5 mL of DCM. The filtrate was evaporated to dryness, and the solid residues were triturated in 10 mL of Et_2O for 15 min, filtered, and washed with 2x 5 mL of Et_2O. Drying of the dark purple solid under vacuum afforded 126 mg of **2** (yield: 89 %), which was shown by ^{1}H NMR to be 98.5 % pure.

Acknowledgements

RTB thanks the NSERC (Discovery grant 2019-05959) and the Canada Research Chairs program for generous financial support and the University of Ottawa, Canada Foundation for Innovation and Ontario Ministry of Economic Development and Innovation for essential infrastructure. The authors thank the SYSPROD project and AXELERA Pôle de Compétitivité for financial support (PSMN Data Center).

Conflict of Interest

The authors declare no conflict of interest.

Data Availability Statement

The data that support the findings of this study (NMR spectra and details of X-ray diffraction and computational chemistry) are available in the supplementary material of this article.

Keywords: Nickel, redox-active N,S ligands, electrochemistry, DFT

[1] R. J. M. K. Gebbink, M.-E. Moret, Eds. *Non-Noble Metal Catalysis: Molecular Approaches and Reactions*, Wiley, 2019.
[2] M. Fritz, S. Schneider, in *The Periodic Table II*, D. M. P. Mingos, Ed., Springer, 2019, pp. 1-36.
[3] M. M. Beromi, C. R. Kennedy, J. M. Younker, A. E. Carpenter, S. J. Mattler, J. A. Throckmorton, P. J. Chirik, *Nat. Chem.* 2021, **13**, 156.
[4] T. Kawamoto, Y. Kushi, *Chem. Lett.* 1992*,* **1992,** 893*.*
[5] T. Kawamoto, H. Kuma, Y. Kushi, *Bull. Chem. Soc. Jpn.* 1997, **70**, 1599.
[6] T. Kawamoto, K. Takeda, M. Nishiwaki, T. Aridomi, T. Konno, *Inorg. Chem.* 2007, **46**, 4239.
[7] D. Herebian, E. Bothe, E. Bill, T. Weyhermüller, K. Wieghardt, *J. Am. Chem. Soc.* 2001, **123**, 10012.
[8] P. Ghosh, A. Begum, E. Bill, T. Weyhermüller, K. Wieghardt, *Inorg. Chem.* 2003*,* **42***,* 3208.
[9] P. Ghosh, A. Begum, D. Herebian, E. Bothe, K. Hildenbrand, T. Weyhermüller, K. Wieghardt, *Angew. Chem. Int. Ed.* 2003, **42***,* 563.
[10] P. Ghosh, E. Bill, T. Weyhermüller, K. Wieghardt, *J. Am. Chem. Soc.* 2003, **125,** 3967.
[11] N. Roy, S. Sproules, E. Bill, T. Weyhermüller, K. Wieghardt, *Inorg. Chem.* 2008, **47***,* 10911.
[12] N. Roy, S. Sproules, E. Bothe, T. Weyhermüller, K. Wieghardt, *Eur. J. Inorg. Chem.* 2009, **2009**, 2655.
[13] S. Sproules, K. Wieghardt, *Coord. Chem. Rev.* 2010, **254,** 1358.
[14] S. Sproules, R. R. Kapre, N. Roy, T. Weyhermüller, K. Wieghardt, *Inorg. Chim. Acta* 2010, **363**, 2702.
[15] S. R. Presow, M. Ghosh, E. Bill, T. Weyhermüller, K. Wieghardt, *Inorg. Chim. Acta* 2011, **374**, 226.
[16] Y. Albkuri, J. S. Ovens, J. Martin, R. T. Baker, *Inorg. Chem.* 2021, **60**, 10934.
[17] K. Fuchigami, M. B. Watson, G. N. Tran, N. P. Rath, L. M. Mirica, *Organometallics* 2021, **40***,* 2283.
[18] P. Chmielewski, M. Grzeszczuk, L. Latos-Grazynski, J. Lisowski, *Inorg. Chem.* 1989, **28***,* 3546.
[19] The formula used for the geometry index is $\tau_4 = 2.55 - 0.00709\cdot(\alpha+\beta)$, where α and β are the largest valence angles around the metal. Originally proposed by: L. Yang, D. R. Powell, R. P. Houser, *Dalton Trans.*1989, 955.
[20] C. L. Wagner, G. Herrera, Q. Lin, C. T. Hu, T. Diao, *J. Am. Chem. Soc.* 2021, **143***,* 5295.
[21](a) F. Neese, *Wiley Interdiscip. Rev.: Comput. Mol. Sci.* 2012, **2**, 73–78. (b) F. Neese, F. *Wiley Interdiscip. Rev.: Comput. Mol. Sci.* 2017, **8**, e1327.
[22](a) J. P. Perdew, M. Ernzerhof, K. J. Burke, *Chem. Phys.* 1996, **105**, 9982; (b) C. Adamo, V. Barone, *J. Chem. Phys.* 1999, **110**, 6158. (c) S. Grimme, J. Antony, S. Ehrlich, H. Krieg, *J. Chem. Phys.* 2010, **132**, 154104.
[23] D. Rappoport, F. Furche, *J. Chem. Phys.* 2010, **133**, 134105.
[24] A. V. Marenich, C. J. Cramer, D. G. Truhlar, *J. Phys. Chem. B* 2009, **113**, 6378.
[25] S. Hirata, M. Head-Gordon, *Chem. Phys. Lett.* 1999, **314**, 291.
[26] Deposition numbers 2227103 (for ***β*-{[2]K(THF)$_2$}$_n$**), 2227104 (for **[2][(18C6)K(THF)]**), 2227105 (for **[2][(18C6)K(THF)$_2$][(18C6)K(THF)(dioxane)$_{0.5}$]**), 2227106 (for **[2]Na(THF)$_3$**), 2227107 (for **{[2]K$_2$(THF)$_{2.5}$}**), 2227108 (for ***α*-{[2]K(THF)$_2$}$_n$**), 2227109 (for **[(N$_2$S$_2$(H))Ni][PPh$_4$]**), 2227110 (for ***β*-1**), and 2285286 (for **[2][Na(THF)$_6$]**) contain the supplementary crystallographic data for this paper. These data are provided free of charge by the joint Cambridge Crystallographic Data Centre and Fachinformationszentrum Karlsruhe Access Structures service.

[27] Bruker. APEX3 Crystallography Software Suite, Bruker AXS Inc., Madison, WI, USA, 2016.
[28] a) G. M. Sheldrick, SADABS, Version 2008/1, 2008. Bruker AXS Inc.,Germany. b) G. M. Sheldrick, APEX-II, SAINT-Plus and TWINABS, 2014, Bruker-Nonius AXS Inc., Madison.
[29] G. M. Sheldrick, *Acta Crystallogr., Sect. A,* 2008, **64**, 112.

Entry for the Table of Contents

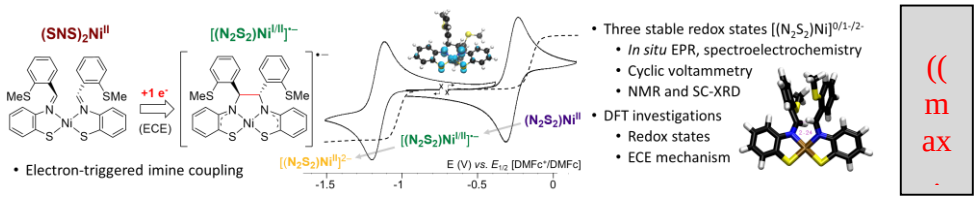

((max. width: 11.0 cm; max. height: 2.5 cm))
1358x295 pixels
Please delete this box prior to submission.

TOC text (50 – 60 words):

Cyclic voltammetry of a bis(imine-thiolate) $Ni(SNS)_2$ complex reveals that one-electron reduction triggers ligand imine C-C bond formation, quantitatively yielding a $[Ni(N_2S_2)]^{\bullet-}$ radical monoanion that can be reversibly oxidized or further reduced to the dianion. Detailed characterization of these three redox states elucidates the redox-active role of the N_2S_2 ligand.

Institute and/or researcher Twitter usernames: ((optional))